Ablation resistance of tungsten carbide cermets under extreme conditions

Samuel A. Humphry-Baker[a,1], Prabhu Ramanujam[b], George D.W. Smith[c], Jon Binner[b] and William E. Lee[d,a]

[a] *Department of Materials, Imperial College London, Prince Consort Road, London, SW7 2BP, UK*
[b] *School of Metallurgy and Materials, University of Birmingham, Edgbaston, Birmingham, B12 2TT, UK*
[c] *Department of Materials, Oxford University, 16 Parks Road, Oxford, OX1 3PH, UK*
[d] *Nuclear Futures Institute, Bangor University, Bangor, LL57 2DG, UK*

ABSTRACT:

A cobalt-free tungsten carbide cermet (WC-FeNi) has been subjected to oxyacetylene flame tests to simulate extreme operating conditions such as a worst-case fusion reactor accident. In such an accident, air-ingress to the reactor may impinge on components operating at surface temperatures in excess of 1000°C, leading to tungsten oxide formation and its subsequent hazardous volatilisation. Here, the most challenging accident stage has been simulated, where the initial air-ingress could lead to extremely rapid air-flow rates. These conditions were simulated using an oxidising oxyacetylene flame. The separation between flame nozzle and sample was varied to permit peak surface temperatures of ~950-1400°C. When the peak temperature was below 1300°C, the cermet gained mass due to the dominance of oxide scale formation. Above 1300°C, the samples transitioned into a mass loss regime. The mass loss regime was dominated by ablation of the scale rather than its volatilisation, which was confirmed by performing a systematic thermogravimetric kinetic analysis. The result was unexpected as in other candidate shielding materials, e.g. metallic tungsten, volatilisation is considered the primary dispersion mechanism. The unusual behaviour of the cermet scale is explained by its relatively low melting point and by the lower volatility of its $FeWO_4$ scale compared to tungsten's WO_3 scale. The substantially lower volatility of the WC cermet scale compared to metallic W indicates it may have a superior accident tolerance.

Keywords:
tungsten carbide cermet, oxyacetylene flame, ablation, oxidation, nuclear fusion, neutron shielding

1. Introduction

Tungsten carbide is a candidate neutron shielding material for fusion reactors due to its combined neutron moderation by carbon and the gamma attenuation of tungsten [1,2]. It's high flexural strength and toughness [3], thermal conductivity [4], sputtering resistance [5] and thermal shock resistance under edge-localised modes [6], also make it a promising candidate plasma facing material. The material also benefits from significant advantages in manufacturability and mechanical properties over other candidate materials such as tungsten, particularly when combined with a metallic binder [7]. The binder metal (commonly Co, Fe, or Ni [8]) enables complex parts to be shaped in the green state and subsequently consolidated to full density by pressureless sintering. It also enables room temperature fracture toughness values of 15-20 MPa $m^{1/2}$ and flexural strengths of 3-4 GPa [9], which exceed the capabilities of metallic tungsten [10]. In recent years, WC-based cermets with Co-free binders have been developed for fusion applications [2,11], and for other extreme environments [12].

In all of the above concepts, WC will activate strongly under neutron irradiation [13], therefore accident safety is a concern. W will form radioactive Re, Os, and Ta and C will

[1] Corresponding author: shumphry@ic.ac.uk

form He and Be via the (n, α) reaction [14] (some ^{14}C will also form, although the amount will be much smaller than from N in steels, e.g. Eurofer'97 [15]). Be is toxic, which presents an added safety concern for a LOCA. The most acute concern in the case of tungsten-based materials is a loss of coolant accident (LOCA) combined with air-ingress into the reactor [16]. In the case of metallic tungsten, the material is expected to operate at surface temperatures in excess of 1000°C in high-heat flux components within a demonstration reactor [17]. If coolant were lost, the temperature could rise further still due to decay heating effects, possibly reaching 1200°C, and remaining above 1000°C for several weeks [18]. At this temperature, tungsten would oxidise readily to form WO_3 which would in turn volatilise at a rate of 0.3 kg/h for every square metre of exposed first wall [19], thus releasing unacceptable quantities of radioactive tungsten, including traces of toxic transmutation products such as Os [20], into the atmosphere. An active area of research is therefore concerned with retarding the oxidation rate of tungsten using alloying additions such as Cr, Y, Ti and Si, and ternary alloys thereof [10,21,22].

The performance of WC-based materials under a LOCA is still relatively poorly understood. While fully-dense monolithic WC appears to show slightly improved oxidation resistance compared to metallic tungsten at 1000°C, WC-cermets show accelerated damage [14,23,24]. A question that remains to be addressed is how the release of hazardous tungsten oxides is affected by rapid air flow rates. Calculations on simulated accident scenarios predict flow rates of 200-300 m/s at points close to the site of air ingress [25]. At such air flow rates, the rate of oxidation – and subsequent volatilisation – would be accelerated, leading to exothermic heat release and possibly further increase in temperature. The oxide scale could also be ablated, thus adding to the speed of its release. It is therefore important that scale ablation, oxidation, and volatilisation are all well understood. For this purpose, oxy-acetylene flame tests can be used. This test allows a sample to be heated to extreme temperatures in an oxidising environment, whilst under high flow rates of the exhaust gas. The test is therefore relevant to simulating the initial stages of a worst-case accident in which vacuum is suddenly lost, whilst the shield is operating at high temperature. The ablation performance of metallic tungsten (and its dispersion strengthened variants) has been widely studied [26–31]. When exposed to temperatures relevant for accident scenarios, the oxide is highly volatile and ablation is not considered a serious concern [26]. However, the situation for WC-based cermets remains unclear.

Here we study ablation of a WC-Fe cermet. An Fe-based binder was selected instead of a more typical Co-based one for several reasons: Co is not considered viable for fusion because of the formation of long-lived ^{60}Co under neutron irradiation; also Co powders are now regarded as carcinogenic; and Co is expensive due to its limited supply chain [12]. Fe by contrast forms relatively benign activation products, mainly Mn and Cr from gas emission [14]. An Fe-based binder might be alloyed either with small additions of Cr, which improves oxidation and irradiation resistance [11], or Ni, which suppresses the formation of the deleterious η-phase [8]. The case of FeNi is studied here, although minor Ni additions will lead to ^{60}Co formation, which may make FeNi disadvantageous as compared to FeCr. Ablation tests were carried out using an oxyacetylene flame. Acetylene was chosen as the laminar burning velocity of acetylene is substantially higher than any other hydrocarbon mixture [32]. The tests were combined with conventional thermogravimetric analysis, which allowed the rates of oxidation and scale volatilisation during ablation tests to be simulated. The analysis shows that ablation initiates when the surface temperature exceeds 1300°C. Volatilisation of the WC-Fe cermet scale is substantially slower than metallic tungsten, which will result in lower release rates in an accident.

2. Experimental methods

2.1. Materials

WC-FeNi cermet samples were obtained from Sandvik Hyperion (Coventry, UK). The cermets contained 90 wt.% WC particles and 10 wt.% FeNi alloy. The WC particles were of the ultra-coarse grade, with a target grain size of 8 μm. The FeNi alloy powders had a composition of 85 wt.% Fe and 15 wt.% Ni. Figure 1 shows a micrograph taken on a polished surface of the cermet, as collected on a Jeol JSM 6010 scanning electron microscope (SEM), operated in back-scattered electron imaging mode. The micrograph shows the WC particles as the light phase and FeNi as the dark phase.

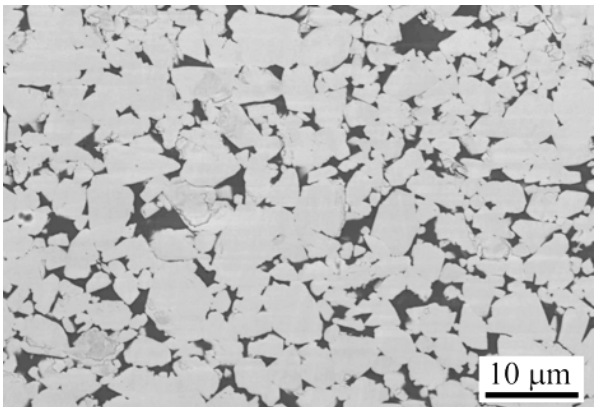

Fig. 1. SEM image of the as-received WC-FeNi cermet, showing a random dispersion of WC grains (light phase) in an FeNi matrix (darker phase).

2.2.Oxyacetylene flame tests

A schematic of the oxyacetylene flame test is shown in Fig. 2. Rectangular samples of dimensions 20 x 6.5 x 5 mm were used. Samples were fixed one at a time in a custom-built water-cooled graphite holder [33], so that their leading face protruded approximately 2 mm. The gas flow rates for the flame were 1.1 m^3/h for oxygen 0.8 m^3/h for acetylene, which yielded an oxidising flame. The nozzle diameter was 1.5 mm, which allowed flame velocities of 223 m/s to be reached at a distance of 10 mm from the nozzle tip [34]. Samples were mounted on a pivoting support, which was swung rapidly into the path of the flame at the beginning of the test. Each test was conducted on a new sample for a fixed time of 300 s. Four tests were conducted in which the separation between the nozzle and sample was 60, 80, 100 and 110 mm, which caused heat fluxes of 3.5, 2.1, 1.3 and 1 MW/m^2, respectively. Details of the heat flux measurements have been reported elsewhere [33]. Hereafter these samples are denoted by the associated heat flux as F3.5, F2.1, F1.3 and F1.0 respectively. The front-facing temperature was recorded using an FLIR Systems Thermovision A40 thermal imaging camera and the temperature at the rear of the sample was recorded using a K-type thermocouple.

All samples were weighed before and after flame testing using a precision microbalance. Sample surfaces were characterised by X-ray diffraction using a Panalytical X'Pert powder diffractometer, with a Cu radiation source. The samples were then cross-sectioned normal to the exposed surface at the centre-point of the sample using a low-speed saw, mounted in epoxy, and polished using conventional metallographic techniques to a finish of 0.05 μm colloidal silica. Cross-sectional images were collected using JEOL JSM 6010 SEM.

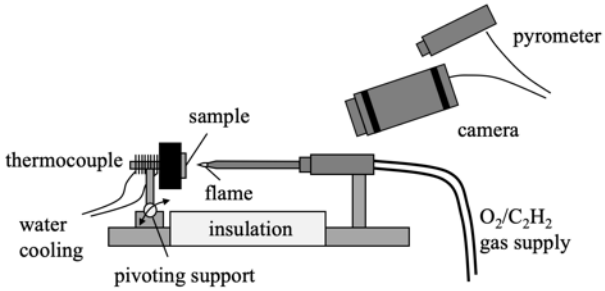

Fig. 2. Schematic of the oxyacetylene flame test.

2.3.Thermogravimetry

Conventional oxidation tests were performed within a Netsch Instruments STA 449 F5 Jupiter thermogravimetric analyser / differential thermal analyser (TGA/DTA). Cuboidal samples of dimensions 5 x 3 x 3 mm were loaded in alumina crucibles and were heated under flowing argon at 10°C/min to the set-points, which were in the range 600-1200°C. Subsequent oxidation experiments were performed by switching purge gas from argon to flowing air (80% N_2 - 20 % O_2), whilst maintaining isothermal conditions. Oxidation mass gain signals were normalised to the evolving sample surface area, using method described in a previous study [23]. The flow rate of air was 100 ml/min unless otherwise specified.

Volatilisation of the oxide scale was also studied in the TGA/DTA using as-oxidised pieces of scale, formed at 800°C and weighing approximately 50 mg. To prevent further oxidation, argon gas was flowed over the samples at 20 ml/min. The latter were heated initially at 50°C/min to 200°C below the isothermal set-point and subsequently at 10°C/min for the remainder. The samples were held at the set-point for durations up to 1 h before cooling.

3. Results

3.1. Oxyacetylene tests

Figure 3(a) shows the temperature profiles of the front face of the samples during the flame tests. In all tests the initial temperature gradient is relatively steep for 1-2 minutes, whereupon it becomes progressively shallower towards the end of the test. The peak temperatures vary from ~950 to ~1400°C, for the lowest and highest heat fluxes conditions. Peak front-facing temperature is recorded in Table 1, along with the peak back-face temperatures, which are generally about 30 % lower.

Figure 3(b) shows side-on photographs of the samples and graphite holder during testing. In F1.0 the sample can be seen to glow yellow, and at higher heat fluxes the sample glows progressively whiter – confirming visually the results from the thermal imaging camera. In the latter tests, the graphite holder also glows red. A flowing stream of gases can be seen around all four samples, but they are particularly prominent for samples F2.1 and F3.5. These clouds were observed to redeposit a layer of yellow/green oxide on the graphite holder around the sample periphery, suggesting significant ablation of the oxide. No such deposits were observed for F1.0 and F1.3.

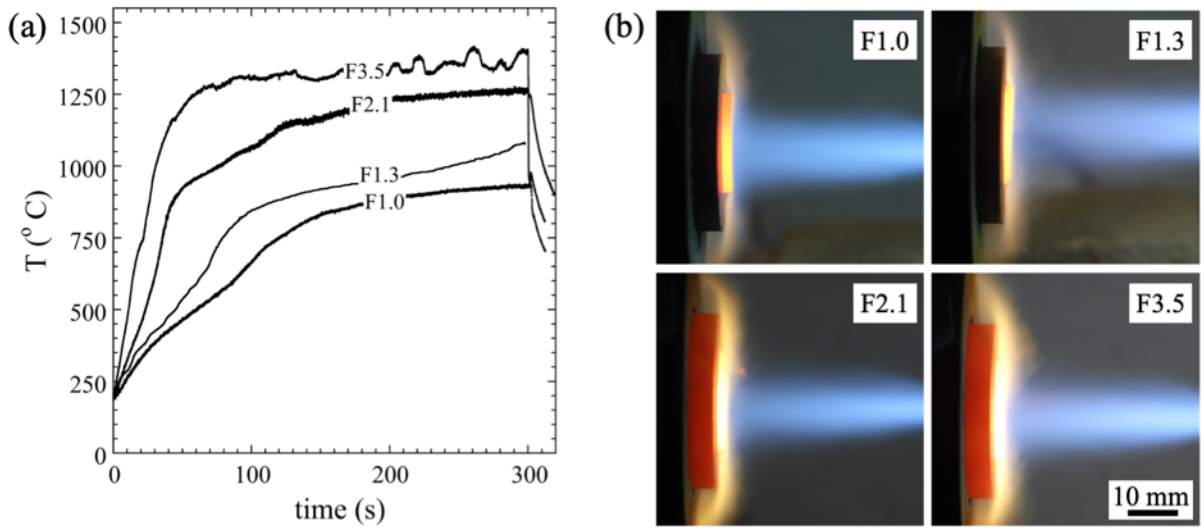

Fig. 3. Characterisation of oxyacetylene flame conditions. (a) Temperature profile of the front face; (b) photographs of samples and gas streams, with visible particle clouds emanating from samples F2.1 and F3.5.

Table 1 shows the changes in sample mass between the start and end of each test. As the heat flux increases from 1 to 2.1 MW/m^2, the mass change increases from 13.5 to 39.9 mg, which can be attributed to increased oxidation because of higher temperature. At 3.5 MW/m^2 the sign of the mass change reverses, due to rate of oxide removal exceeding its rate of formation. Note – although some oxide was observed to redeposit on the graphite holder for sample F2.1 as well, the overall positive mass gain suggests the overall rate of evaporation and redeposition rate was small compared to the rate of stable surface oxide formation.

Table 1
Heat flux, peak temperatures and mass change during oxyacetylene flame tests.

Sample	Distance (mm)	Heat Flux (MW/m^2)	T_{peak} front (°C)	T_{peak} back (°C)	Mass change (mg)
F1.0	110	1.0	938	650	13.5
F1.3	100	1.3	1092	687	25.6
F2.1	80	2.1	1277	784	39.9
F3.5	60	3.5	1417	961	-41.3

Figure 4 shows the identified the phases formed after flame exposure and their morphology. Part (a) shows XRD patterns. For lower heat flux samples, F1 and F1.3, only the WO_3 phase is visible, as indicated by the indexed powder diffraction standard shown above the F1.0 diffraction pattern. In F2.1 and F3.5, $FeWO_4$ is also formed, as shown by the indexed powder diffraction standard below the F3.5 pattern. As the heat flux increases from F2.1 to F3.5, the proportion of $FeWO_4$ increases. This increase is likely due to preferential volatilisation of WO_3, due to its higher vapour pressure than iron oxides (10^{-3} atm is reached is ~1560K for WO_3 and ~2300 K for FeO [35]). Part (b) shows the corresponding SEM images: The scale in F1.0 and F1.3 is composed of very fine grains of WO_3, ~1-2 µm across, while the mixed WO_3-$FeWO_4$ scales contain very large $FeWO_4$ crystals (~20 µm at F.21 and (200 µm at F3.5). It is interesting to note that the lath-like crystals in F3.5 are associated with an increase in c-axis texture in the X-ray data – notably the (020) and (200) increase

substantially relative to the diffraction standard.

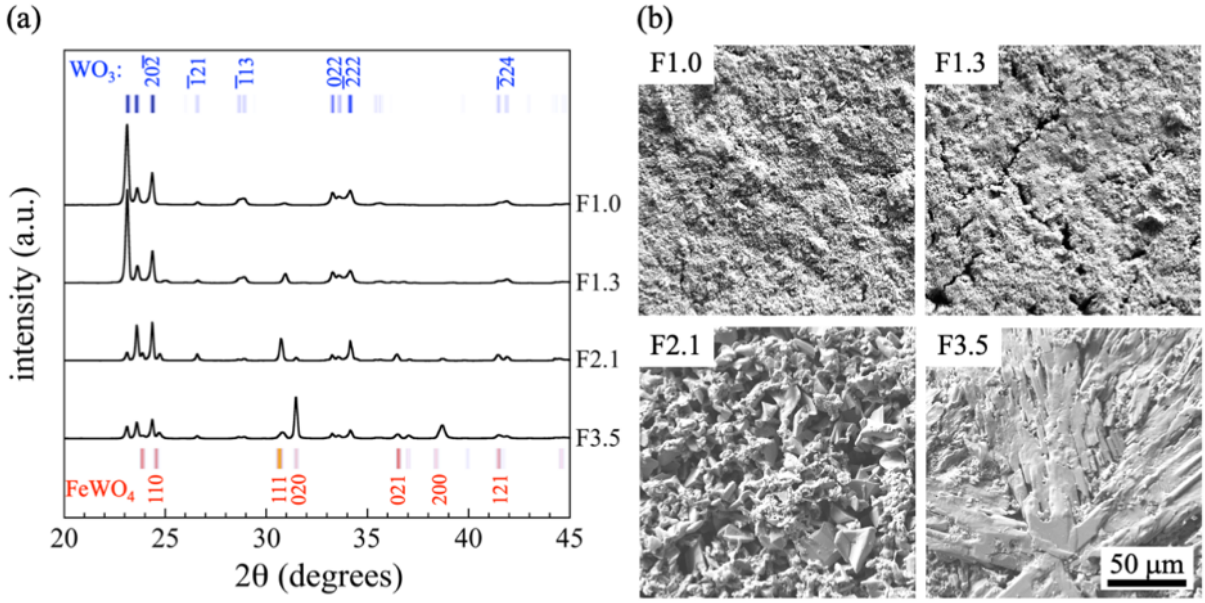

Fig. 4. Flame tested oxide scales change from WO_3 to $FeWO_4$ between F1.3 and F2.1, as shown in (a) X-ray diffractograms, and (b) SEM micrographs (taken in secondary electron imaging mode) of the same area. Scale is same for all images.

Figure 5 shows SEM cross sectional images of the samples after testing, with corresponding photographs in the upper-right inset. In all SEM micrographs, a porous oxide scale is observed on the front-facing surface. For samples F1.0 to F2.1, the oxide thickness increases monotonically with increasing heat flux, from ~50 µm for the F1.0 sample to ~160 µm for F2.1. However, for sample F3.5, the oxide thickness is only 50 µm. This observation is agreement with the decrease in mass change in Table 1, suggesting that significant amounts of oxide were either evaporated or ablated from the surface.

Direct evidence of oxide ablation can be seen by comparing the front- and side-facing oxide scale thicknesses in Figure 5. Those in samples F1.0 and F1.3 are homogeneous, however in F2.1 and F3.5 there is a greater degree of scale build-up on the sides. In F2.1 the side of the scale is approximately 300 µm thick and extends about ~2 mm down. This indicates that a directional flow of partially liquid oxide has occurred, driven by the pressure of the incoming gas jet. The flow of oxide was even more significant in sample F3.5, where the side scale built up much further down from the leading edge, with a thickness of ~500 µm at its maximum. This is seen more clearly in the upper right inset, which shows a continuous collar of oxide around the entire periphery of the sample, again extending about 2 mm down, coinciding with where the sample protruded from the graphite block. The fact that material adjacent to the graphite block is not ablated suggests there is a dead zone in the airflow, where the oxide could accumulate.

The magnified regions of the scales in the lower-right inset (taken in back-scattered electron imaging mode) reveal some important chemical inhomogeneities in the scale. While F1.0 and F1.3 show a homogeneous scale, F2.1 shows two distinct phases, light and dark. This is consistent with the single phase WO_3 diffraction pattern in F1.0 and F1.3 and the mixed $WO_3 + FeWO_4$ pattern in F2.1 (Fig. 4). In the F3.5 sample, the leading edge was heavily ablated, and no clear phase separation was seen, however the oxide that accumulated adjacent to the graphite block was very distinctly phase separated. The inset shows the dead zone in airflow has led to a darker oxide, i.e. $FeWO_4$ on the exterior, with a gradual transition towards a mixed WO_3 plus $FeWO_4$ oxide on the interior. This again supports the idea that

during exposure, some WO_3 is preferentially removed from the surface region due to volatilisation.

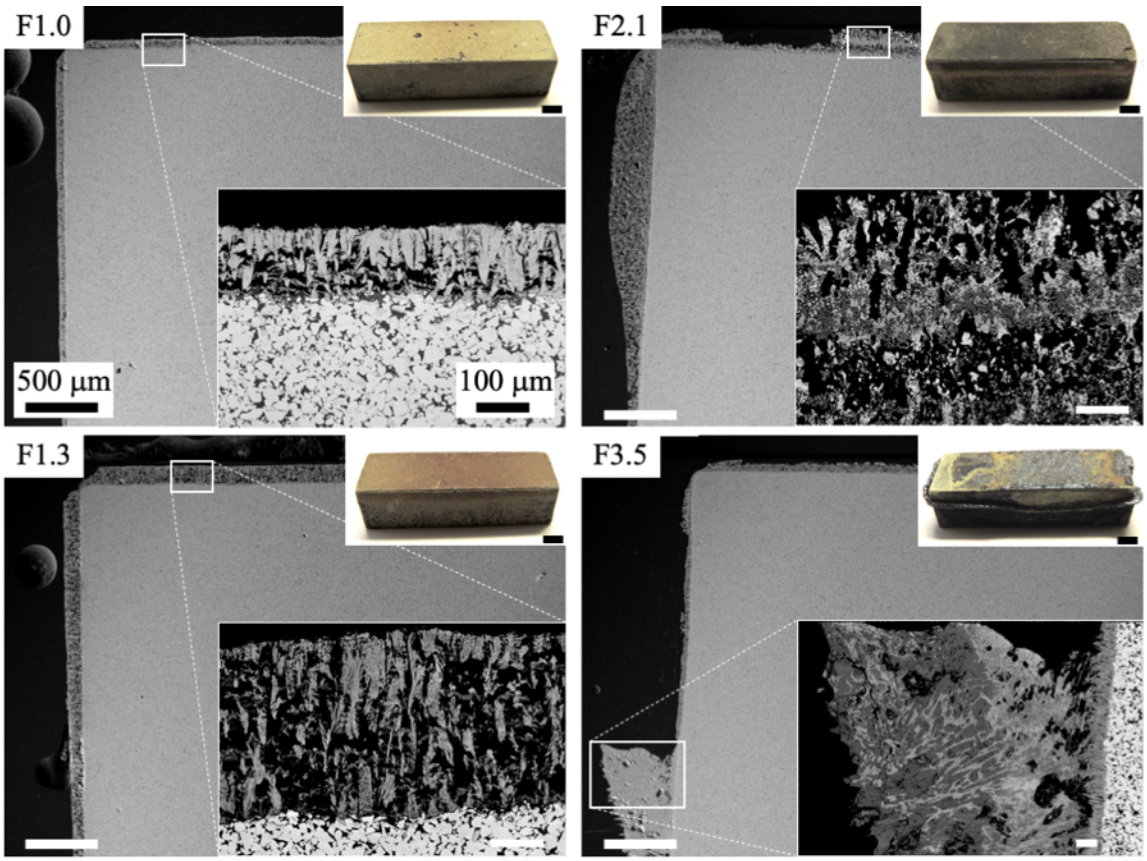

Fig. 5. Cross-sectional SEM micrographs of the oxide coatings at the front and side faces (scale bar is 500 µm for all). Upper inset: optical photographs of sample (scale bar is 1 mm). Lower inset: high magnification images (scale bar is 100 µm for all).

3.2. Oxidation rate constants

Figure 6 shows the oxidation rates of the material in the TGA experiments. Part (a) shows the raw mass gain signals as a function of temperature. Linear kinetics are observed, suggesting the scale is not protective, which is consistent with previous works [23,36]. Part (b) shows the corresponding oxidation rate constants, as calculated from the gradient of the lines in part (a). The rate constants appear to show two regimes of behaviour, a low temperature regime below 800°C, with an activation energy of 206 kJ/mol, and a high temperature regime at 800°C and above, with an activation energy of 32 kJ/mol.

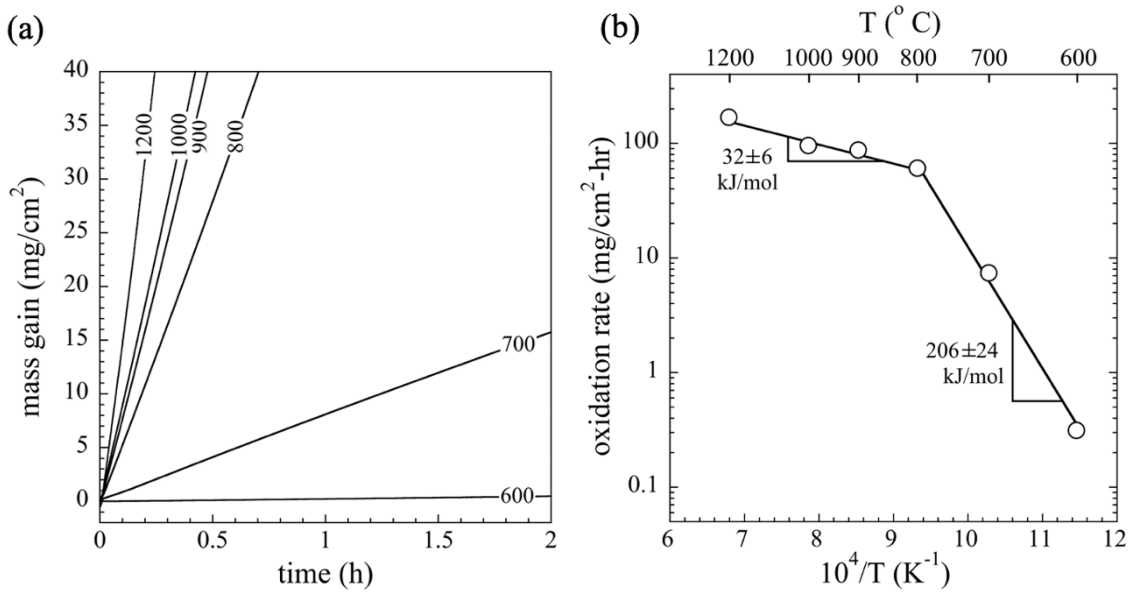

Fig. 6. Oxidation kinetics, (a) raw mass gain signals from TGA and (b) rate constants as determined from the gradient of the line. Activation energy error represents the maximum deviation from removal of any one data-point.

Figure 7 shows the effect of the air flow rate in the TGA. The data has been fitted with a linear relationship between the oxidation rate and the natural logarithm of the flow rate, which appears to agree with the experimental data well. Combining observations in Figs 6 and 7, an expression for the high temperature regime's oxidation rate, M_{Ox}, can be written as a function of temperature, T and flow rate, f:

$$M_{Ox} = 489 \ln f \exp\left(-\frac{32{,}200}{RT}\right)$$

where R is the molar gas constant.

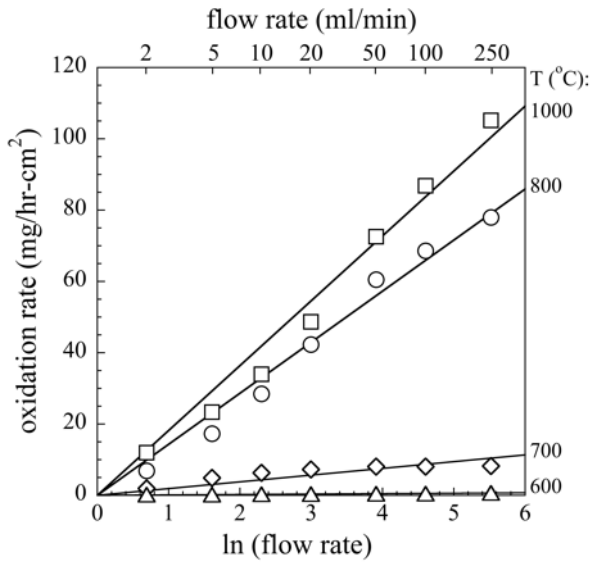

Fig. 7. Effect of air flow rate on oxidation rate constants.

3.3. Volatilisation rate constants

Figure 8 shows the typical mass loss signal during an oxide volatilisation experiment carried out in flowing argon gas. The data is restricted to the final portion of the heating profile (>1000°C) for clarity. The upper line, plotted on the secondary y-axis, show the sample being heated to the set-point temperature of 1200°C and being held for 30 minutes. The other two datasets, plotted on the primary y-axis, represent the DTA signal, and the mass change signal. The DTA signal shows a clear endothermic peak at ~35 minutes, corresponding to 1103°C. The peak temperature is in good agreement with the available experimental data for melting of mixed iron-tungsten oxides. A vertical section of the Fe_2O_3 – WO_3 phase diagram shows that the peritectic melting temperature for Fe_2WO_6, is 1100°C [37]. No equivalent vertical section is available in the literature for FeO-WO_3, but our observation of a DTA peak at 1103°C suggests that $FeWO_4$ melts at a similar temperature to Fe_2WO_6. This indication that the scale had partially melted was confirmed by visually inspecting the samples after the DTA tests. In samples treated at 1100°C or above the scale pooled in the bottom of the crucible, which was clear evidence of scale melting. After the set-point is reached, the mass decreases linearly due to scale evaporation, with a gradient denoted M_{Ev}.

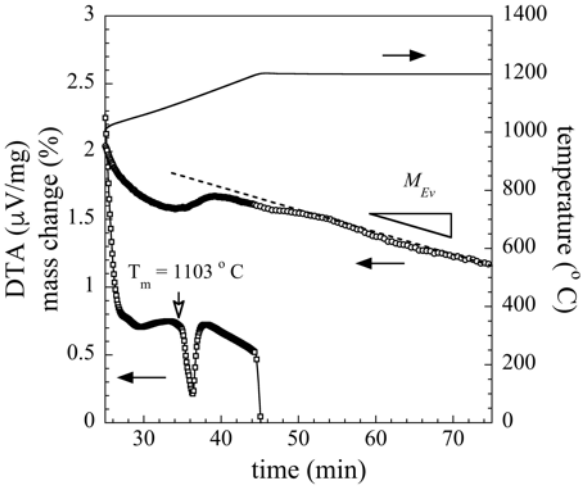

Fig. 8. The evolution in DTA signal (lower signal, in squares), mass change (middle, circles) and temperature (solid line) during a typical volatilisation experimental.

Figure 9 re-plots the isothermal mass change on a positive scale. The data is normalised by the specimen surface area and includes other temperatures, at 50°C increments from 1050 to 1300°C. Part (a) shows the raw mass loss curves, fitted with lines through the origin. The gradient of these lines, i.e. rate constants, M_{Ev}, are plotted in part (b) as a function of inverse temperature. The data evaporation rate can be fitted by the following Arrhenius equation:

$$M_{Ev} = 4.52 \times 10^{13} \exp\left(-\frac{367{,}000}{RT}\right)$$

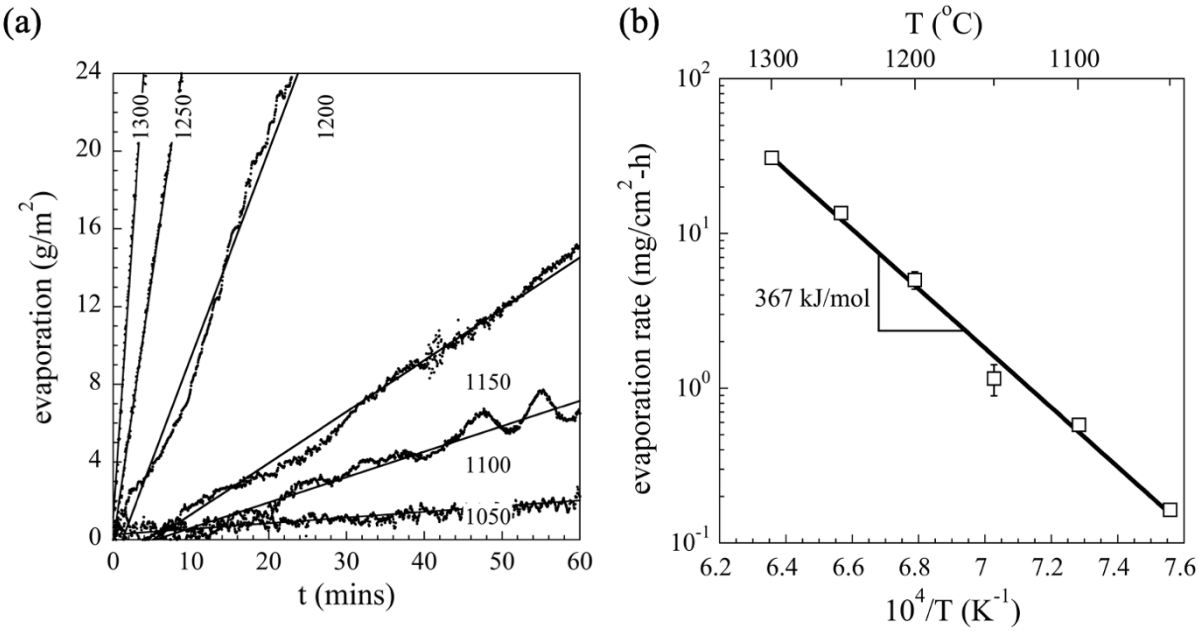

Fig. 9. Scale evaporation, (a) raw evaporation data as a function of temperature; (b): linear rate constants as a function of inverse temperature, fitted by an Arrhenius law. Error bars represent gradient change when only initial half of data is fitted.

4. Discussion

The goal of this study was to determine the rates of ablation and volatilisation during accident scenarios involving high air-flow rates, and to compare these to metallic tungsten. This was complicated by three simultaneous processes contributing to the sample mass loss during the oxyacetylene tests. To separate the contribution of each, we begin by simulating the oxide formation and volatilisation rates during the oxyacetylene flame test, using TGA-derived evaporation rates reported in section 3.2. Comparing the measured mass loss to the volatilised mass loss, allows us to estimate the degree of ablation. Second, we comment on the material's likely performance in real accident scenarios given the likely air-flow rates in an accident. Finally, we compare the anticipated performance to that of metallic tungsten.

4.1. Scale simulations using thermogravimetry-derived kinetics

To determine the dominant mechanism of mass loss, we first simulate the degree of oxidation and volatilisation using the evaporation rates derived from thermogravimetry in section 3.2. This is done by combining these data with the temperature evolution curves in Fig. 3(a). The comparison between such simulations and the experimental observed mass changes enables the degree of ablation to be quantified.

Beginning with oxide formation, its instantaneous rate can be calculated using equation (1), where the flow rate is taken to be the overall flow rate of gas through the flame nozzle, i.e. f=1.9 m^3/h. The exposed area for oxidation is taken to be 104.5 mm^2, by assuming a front area of 52.5 mm^2 and a side area of 52 mm^2, which are in turn calculated from the 10 x 6.5 mm front face and 2 mm protrusion from the block. The oxidation rate at each temperature during the test is then integrated over time.

Next, oxide volatilisation can be simulated in the same way by applying equation (2), assuming that the area of oxide available for volatilisation is the same as that available for

oxidation (note: the volatilisation rate is assumed to be independent of flow rate, as confirmed experimentally in the thermogravimetric tests).

Figure 11(a) shows the predicted evolution in oxide formation and volatilisation. As expected, the oxide formation curves become steeper with increasing heat flux. The gradient of the curves generally increases with time due to the rising temperature, approaching linearity as the temperature (c.f. Figure 3) begins to plateau. By comparison, the predicted degree of volatilisation is near zero for F1.0 and F1.3, while in F2.1 and F3.5 it is significant (0.4 mg/cm^2 and 3.4 mg/cm^2 respectively). Figure 11(b) plots the endpoints reached in Figure 11(a) alongside experimental mass change data. The simulated oxide evolution is shown in triangles – formation symbols point upwards, and volatilisation downwards. The overall balance between these is shown as open diamonds, and the figure for comparison, measured mass change, is shown as closed diamonds.

There is relatively good agreement between the experiments and predictions for F1.0, F1.3 and F2.1. The predicted values are about 15-25% lower than the measured values (e.g. for F2.1 these are 23 and 31 mg/cm^2 respectively). The fact that the predicted values are slightly lower is probably due to the presence of some additional oxidation on the back-face of the sample, which is not accounted for in the simulations. It is also possible that the presence of carbon in the flame plays a role, due to the formation of CO and CO_2 during acetylene combustion [32]. The production of CO and CO_2 from carbon present in the cermet could also lead to some discrepancy, however the effect is expected to be minor considering the molar mass of these gases is small compared to WO_3 or $WFeO_4$.

The agreement between experiment and predictions breaks down for the F3.5 sample; the predicted and measured values have different signs (28 mg/cm^2 and -32 mg/cm^2, respectively). Therefore, some other mechanism of material removal not accounted for in the simulations must be in operation. The cloud formations (Fig. 3) and heavily depleted front facings scales (Fig. 5), coupled with the observations of deposited oxide scales on the graphite holder at the highest heat fluxes, suggest that this discrepancy is due to ablation of the scale. This conclusion is also consistent with the surface temperature measurements (Fig. 3), which show that the scale surface far exceeded 1100°C and was therefore likely in the liquid state. The ablation of liquid oxide could therefore easily be driven by the increased air pressure of the flame.

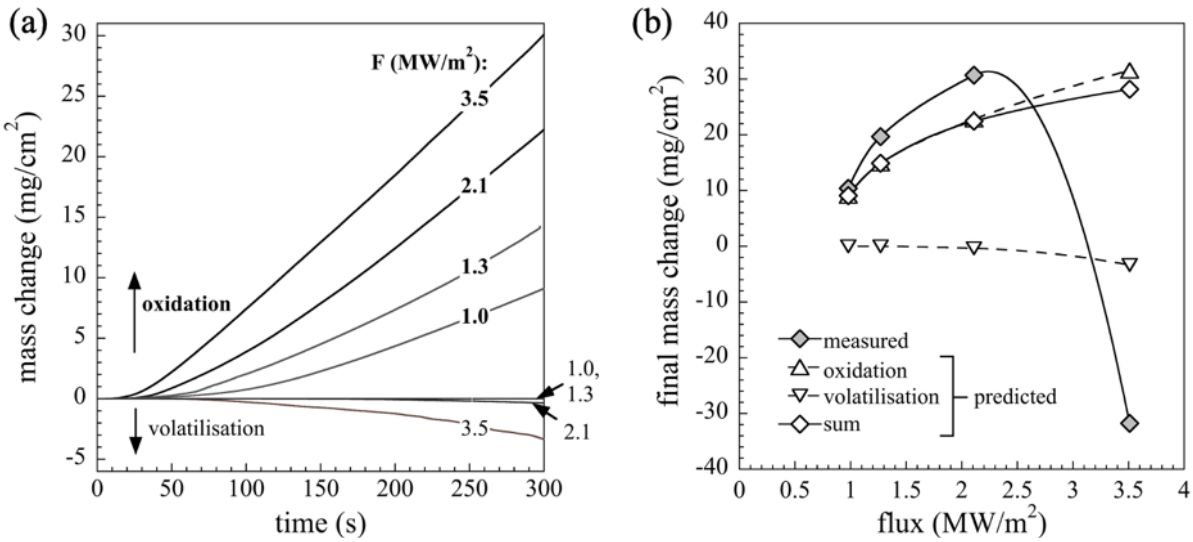

Fig. 10. Scale simulations using during oxyacetylene flame tests from TGA-derived kinetic laws, (a) oxide formation and volatilisation at each heat flux; (b) final simulated mass changes (open symbols) compared to the measured data (closed symbols).

4.2. Relevance to an accident scenario

To relate our results to likely conditions experienced in the early stages of a fusion reactor accident scenario, it is important to compare the likely gas flow rates with those during the flame tests. Previous work in our team has shown the gas velocity at a distance of 10 mm from the nozzle to be 223 m/s [34]. To predict the flow rates at the nozzle separations used in this study, we use data from Ozturk and Cetegen [38], who systematically vary air flow rates as a function of distance from the nozzle. At a nozzle flow rate of 0.60 m^3/h and 10mm separation, they reported a flow rate of 76 m/s. If this velocity is scaled by the difference in flow rates (1.9 here vs. 0.6 m^3/h in their study), this equates to a flow rate of 241 m/s, which is in good agreement with this study. At 60 mm separation, i.e. comparable to the F3.5 test, Ref. [38] reported gas velocity of between 17 and 21 m/s for experiments and calculations, respectively. Again, using the scaling argument above due to the differences in nozzle flow rates, we estimate that our flow rates would be on the order of 54-66 m/s. These velocities are significantly less than those predicted during a loss-of-vacuum accident in a fusion reactor, which could be as high as 200-300 m/s during the initial stages [25].

The fact that realistic air flow rates in the initial accident stages may exceed those in this study suggests that ablation could be an important mechanism of dispersal. Thus, we envisage two stages during an accident with different dispersion mechanisms: (1) Ablation stage, when flow rates of several hundred m/s may be possible during the first few seconds after air-ingress; and (2) Volatilisation stage, where more stable air-flow conditions are expected. The ablation and volatilisation stages are discussed in sections 4.3 and 4.4 by comparing to metallic tungsten.

4.3. Primary accident stage: ablation

We now address the primary accident stage, where the shield remains at high operational temperatures and therefore could be ablated by rapid air ingress. It is useful to compare the ablation results of this study to previous work on metallic tungsten, which is the leading candidate material for plasma-facing surfaces (summarised in Table 2). Previous work was performed at nozzle-sample separations of 10-20 mm, i.e. much shorter than the 60-110 mm used in this study. The heat fluxes are therefore expected to be much higher; although these values were not reported, this is implied from the increased temperature rises (typically 600-1000°C more than the present study). As a result, these studies generally found much greater mass loss rates than the present study – up to a factor of 1000 in the case of Ref. [28]. The accelerated mass loss is likely due to the higher temperatures and air flowrates at the sample surface.

Table 2
Literature studies of oxyacetylene flame testing on tungsten-based materials

Author [Ref]	Material	Nozzle-sample separation (mm)	O_2 flow rates (m^3/h)	Test duration (s)	Peak temperature (°C)	Mass change rate (mg/s)
Mass loss regime						
Lee [28]	W	20	0.72	60	2300	141
Umer [27]	W	20	0.6	30-60	2400	93-111
Guo [26]	W coatings on C/C	10	1.52	20 to 30	/	0.57-4.1

Song [31]	W	10	1.5	30-120	2000	39-50
this study	WC-FeNi	60	1.1	300	1417	0.14
Mass gain regime						
Guo [26]	W coatings on C/C	10	0.88	20-60	/	0.01-0.54
this study	WC-FeNi	80-110	1.1	300	938-1277	0.05-0.13

The exception in Table 2 is the work by Guo *et al.* [26] who also report a transition from mass gain to mass loss with increasing heat flux – i.e. a similar transition to the present study. The transition was induced by increasing the flow rate of oxygen from 0.88 to 1.52 m^3/h, with a corresponding increase in heat flux from 2.4 to 4.2 kW/m^2. The gain-loss transition therefore occurred in a similar range of heat fluxes to the present study (2.1-3.5 kW/m^2). The key difference between our study and Guo *et al.* was the shorter nozzle-sample separation, 10 mm, which would have produced a more localised heat flux and thus higher local temperature rise. Although the researchers did not report temperature rise, the conditions used were similar to Song *et al.*, who reported a temperature rise of ~2000°C [31]. It is therefore reasonable to assume that the temperature rise required to induce ablation is likely higher for W than for WC-FeNi.

The improved ablation resistance in W is likely due to the higher melting point of its oxide scale. Pure WO_3 melts at 1474°C, which is higher than the melting transition observed in the present study (~1100°C according to Fig. 8), meaning W can accommodate significantly higher temperatures before being thermally ablated. This suggests that in the initial accident stage considered here, the oxide scale of W would not be ablated unless the surface temperature exceeded 1474°C. Second, pure W has a higher thermal conductivity than WC-FeNi. The room temperature thermal conductivity of WC cermets is typically in the range 90-140 W/m-K [39], which is slightly lower than that of pure W (~160 W/m-K [26,27,31]). Therefore, the temperature rise experienced on metallic W is expected to be lower for a given heat flux.

The above factors suggest some possible routes towards improving the ablation resistance of WC based materials: First, thermal conductivity could be improved by increasing the WC grain size [39,40]. However, while it may lower the surface temperature in an oxyacetylene flame test, it is not clear what the effect of improved thermal conductivity would be during a real accident scenario, where the temperature rise has been modelled solely based on internal heat production from radioactive decay [18], and surface heat flux due to the exothermic heating of the oxidation reaction is neglected. A rigorous quantitative comparison of the surface and volumetric heating is required in order to elucidate this. Second, it may be fruitful to use a functionally graded material, or a cemented carbide coated with a more ablation-resistant outer layer. Impregnation with silicon [36] and boron [41] have proved effective in improving the oxidation resistance of cermets. Ablation tests on such coated structures are needed.

4.4. Secondary accident stage: volatilisation

We now address the second stage of the accident scenario, where air flow rates will be stable, and components might be slowly reheated to ~1200°C due to activation heat and remain above 1000°C for several weeks [18]. In this scenario WC-FeNi may have an advantage in terms of its resistance to volatilisation. Fig. 11 shows the evaporation rate of the mixed WO_3-$FeWO_4$ scale compared to pure WO_3, data for which is taken from Wegener et al [19] and Blackburn et al [42]. The plot shows significantly lower evaporation rates of WC-

FeNi scales are expected. Over the temperature range studied, the evaporation rate is about a factor of 10 lower than tungsten. This suggests that while WC-FeNi scales may be dispersed faster during the initial stages of the accident, as the accident progresses and more stable air-flow conditions are reached, the material may disperse less material in the long run.

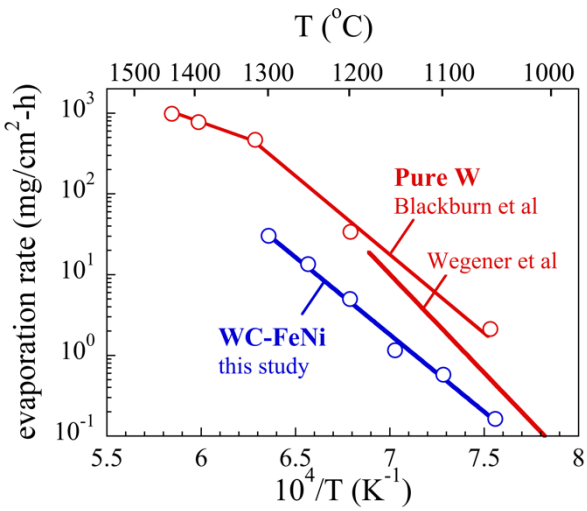

Fig. 11. Comparison of evaporation rate of the mixed WO_3-$FeWO_4$ scale (blue) with pure WO_3 (red) [19,42].

5. Conclusions

A candidate WC-based neutron shielding material has been tested in an oxyacetylene flame to simulate high air flows that may be experienced in a worst-case fusion reactor loss-of-vacuum accident scenario, whilst operating at high temperature. When the peak temperature was 1300°C or less, the sample gained mass due to the dominance of oxide scale formation. Above this point the sample transitioned into a mass loss regime. By simulating the rates of volatilisation using thermogravimetry-derived kinetic laws, the majority of mass loss was attributed to ablation due to melting of the oxide scale above 1100°C.

This result implies that if WC-based cermets are to be employed as plasma-facing materials, ablation could be a significant mechanism of material dispersion during the early stages of an accident. Once the air-flow settles, dissemination would become dominated by volatilisation, which is much slower.

Compared to metallic tungsten, WC-FeNi shows lower resistance to ablation. This is explained by a lower melting point of the $FeWO_4$ scale compared to WO_3. On the other hand, WC-FeNi shows a higher resistance to volatilisation. This indicates that while WC-based cermets may disperse more material during the initial stages of an accident, they will become more stable over the long term. The increased long-term stability of WC-based cermets compared to metallic W is an encouraging development and indicates they could be dispersed at a substantially slower rate in an accident.

From a fusion engineering perspective, this study shows the importance of considering the resistance to ablation when assessing the safety of a tungsten-based plasma facing materials, since usually materials are ranked primarily on their damage resistance under static oxidation. More work is needed to determine the ablation resistance of leading tungsten-based candidate materials under more realistic heat and air fluxes.

Acknowledgements

We acknowledge EPSRC support through grant EP/K008749/1 Materials Systems for Extreme Environments. Tokamak Energy Ltd. was an Industrial Partner in this project. We would also like to thank Virtudes Rubio, University of Birmingham, for assisting with oxyacetylene flame tests and Jessica. M. Marshall, Sandvik Hyperion, for providing the WC-FeNi cermet used in this study.

Declaration of interest

GDWS, WEL and SHB are paid consultants to Tokamak Energy Ltd.

References

[1] C.G. Windsor, J.G. Morgan, P.F. Buxton, A.E. Costley, G.D.W. Smith, A. Sykes, Modelling the power deposition into a spherical tokamak fusion power plant, Nuclear Fusion. 57 (2016) 036001. https://doi.org/10.1088/1741-4326/57/3/036001.

[2] C. Windsor, J.M. Marshall, J.G. Morgan, J. Fair, G.D. Smith, A. Rajczyk-Wryk, J. Tarrago, Design of cemented tungsten carbide and boride-containing shields for a fusion power plant, Nuclear Fusion. 58 (2018) 076014.

[3] L. Silvestroni, N. Gilli, A. Migliori, D. Sciti, J. Watts, G.E. Hilmas, W.G. Fahrenholtz, Binderless WC with high strength and toughness up to 1500° C, Journal of the European Ceramic Society. (2020).

[4] A. Gubernat, P. Rutkowski, G. Grabowski, D. Zientara, A. Gubernat, P. Rutkowski, G. Grabowski, D. Zientara, Hot pressing of tungsten carbide with and without sintering additives, International Journal of Refractory Metals and Hard Materials. (2014) 193–199.

[5] H. Plank, W. Eckstein, Preferential sputtering of carbides under deuterium irradiation—a comparison between experiment and computer simulation, Nuclear Instruments and Methods in Physics Research Section B: Beam Interactions with Materials and Atoms. 124 (1997) 23–30.

[6] S.A. Humphry-Baker, G.D.W. Smith, G. Pintsuk, Thermal shock of tungsten carbide in plasma-facing conditions, Journal of Nuclear Materials. 524 (2019) 239–246. https://doi.org/10.1016/j.jnucmat.2019.06.041.

[7] L. Prakash, 1.02 - Fundamentals and General Applications of Hardmetals, in: V.K. Sarin (Ed.), Comprehensive Hard Materials, Elsevier, Oxford, 2014: pp. 29–90. https://doi.org/10.1016/B978-0-08-096527-7.00002-7.

[8] C.M. Fernandes, A.M.R. Senos, Cemented carbide phase diagrams: a review, International Journal of Refractory Metals and Hard Materials. 29 (2011) 405–418.

[9] T. Sailer, M. Herr, H.-G. Sockel, R. Schulte, H. Feld, L.J. Prakash, Microstructure and mechanical properties of ultrafine-grained hardmetals, International Journal of Refractory Metals and Hard Materials. 4 (2001) 553–559.

[10] C. Linsmeier, M. Rieth, J. Aktaa, T. Chikada, A. Hoffmann, J. Hoffmann, A. Houben, H. Kurishita, X. Jin, M. Li, Development of advanced high heat flux and plasma-facing materials, Nuclear Fusion. 57 (2017) 092007.

[11] S.A. Humphry-Baker, R.W. Harrison, G. Greaves, A.J. Knowles, G.D.W. Smith, S.E. Donnelly, W.E. Lee, A candidate fusion engineering material, WC-FeCr, Scripta Materialia. 155 (2018) 129–133. https://doi.org/10.1016/j.scriptamat.2018.06.027.

[12] J.J. Pittari III, H.A. Murdoch, S.M. Kilczewski, B.C. Hornbuckle, J.J. Swab, K.A. Darling, J.C. Wright, Sintering of tungsten carbide cermets with an iron-based ternary alloy binder: Processing and thermodynamic considerations, International Journal of Refractory Metals and Hard Materials. 76 (2018) 1–11.

[13] S.X. Oliver, M.L. Jackson, P.A. Burr, Radiation-induced evolution of tungsten carbide in fusion reactors: accommodation of defect clusters and transmutation elements, ACS Applied Energy Materials. 3 (2019) 868–878. https://doi.org/10.1021/acsaem.9b01990.

[14] S.A. Humphry-Baker, G.D. Smith, Shielding materials in the compact spherical tokamak, Philosophical Transactions of the Royal Society A. 377 (2019) 20170443.
[15] V.I. Khripunov, D.K. Kurbatov, M.L. Subbotin, Carbon-14 Source Terms and Generation in Fusion Power Cores, J Fusion Energ. 27 (2008) 241–249. https://doi.org/10.1007/s10894-008-9145-2.
[16] M. Lukacs, L.G. Williams, Nuclear safety issues for fusion power plants, Fusion Engineering and Design. 150 (2020) 111377. https://doi.org/10.1016/j.fusengdes.2019.111377.
[17] J.H. You, E. Visca, T. Barrett, B. Böswirth, F. Crescenzi, F. Domptail, M. Fursdon, F. Gallay, B.-E. Ghidersa, H. Greuner, M. Li, A. v. Müller, J. Reiser, M. Richou, S. Roccella, Ch. Vorpahl, European divertor target concepts for DEMO: Design rationales and high heat flux performance, Nuclear Materials and Energy. 16 (2018) 1–11. https://doi.org/10.1016/j.nme.2018.05.012.
[18] D. Maisonnier, I. Cook, S. Pierre, B. Lorenzo, B. Edgar, B. Karin, D.P. Luigi, F. Robin, G. Luciano, H. Stephan, N. Claudio, N. Prachai, P. Aldo, T. Neill, W. David, The European power plant conceptual study, Fusion Engineering and Design. 75–79 (2005) 1173–1179. https://doi.org/10.1016/j.fusengdes.2005.06.095.
[19] T. Wegener, F. Klein, A. Litnovsky, M. Rasinski, J. Brinkmann, F. Koch, C. Linsmeier, Development of yttrium-containing self-passivating tungsten alloys for future fusion power plants, Nuclear Materials and Energy. 9 (2016) 394–398.
[20] M.R. Gilbert, J.-C. Sublet, Neutron-induced transmutation effects in W and W-alloys in a fusion environment, Nuclear Fusion. 51 (2011) 043005.
[21] S. Telu, A. Patra, M. Sankaranarayana, R. Mitra, S.K. Pabi, Microstructure and cyclic oxidation behavior of W–Cr alloys prepared by sintering of mechanically alloyed nanocrystalline powders, International Journal of Refractory Metals and Hard Materials. 36 (2013) 191–203. https://doi.org/10.1016/j.ijrmhm.2012.08.015.
[22] C. García-Rosales, P. López-Ruiz, S. Alvarez-Martín, A. Calvo, N. Ordás, F. Koch, J. Brinkmann, Oxidation behaviour of bulk W-Cr-Ti alloys prepared by mechanical alloying and HIPing, Fusion Engineering and Design. 89 (2014) 1611–1616. https://doi.org/10.1016/j.fusengdes.2014.04.057.
[23] S.A. Humphry-Baker, W.E. Lee, Tungsten carbide is more oxidation resistant than tungsten when processed to full density, Scripta Materialia. 116 (2016) 67–70. https://doi.org/10.1016/j.scriptamat.2016.01.007.
[24] M. Aristizabal, N. Rodriguez, F. Ibarreta, R. Martinez, J.M. Sanchez, Liquid phase sintering and oxidation resistance of WC–Ni–Co–Cr cemented carbides, International Journal of Refractory Metals and Hard Materials. 28 (2010) 516–522. https://doi.org/10.1016/j.ijrmhm.2010.02.010.
[25] C. Bellecci, P. Gaudio, I. Lupelli, A. Malizia, M. Porfiri, R. Quaranta, M. Richetta, CFD Analysis of loss of vacuum accident for safety application in experimental fusion reactor facility, in: COMSOL 2009, 2009.
[26] L. Guo, J. Peng, C. Guo, C. Huo, R. Sun, Y. Zhang, Ablation performance of supersonic atmosphere plasma sprayed tungsten coating under oxyacetylene torch and plasma torch, Vacuum. 143 (2017) 262–270.
[27] M.A. Umer, D. Lee, H.J. Ryu, S.H. Hong, High temperature ablation resistance of ZrNp reinforced W matrix composites, International Journal of Refractory Metals and Hard Materials. 42 (2014) 17–22.
[28] D. Lee, M.A. Umer, H.J. Ryu, S.H. Hong, Elevated temperature ablation resistance of HfC particle-reinforced tungsten composites, International Journal of Refractory Metals and Hard Materials. 43 (2014) 89–93.
[29] D. Wang, Y. Wang, B. Wei, S. Huo, G. Song, Y. Zhou, Effect of W content on the ablation properties of W-ZrC composites synthesized by reactive melt infiltration under oxyacetylene flame, International Journal of Refractory Metals and Hard Materials. 74 (2018) 28–39.
[30] G. Song, Y. Wang, Y. Zhou, Carbide Particle-Reinforced Tungsten Composites in Extreme Hazard Environments: Ablation, Thermal Shock, and Finite Element Calculation, in: MAX Phases and Ultra-High Temperature Ceramics for Extreme Environments, IGI Global, 2013: pp. 509–532.

[31] G.M. Song, Y.J. Wang, Y. Zhou, Elevated temperature ablation resistance and thermophysical properties of tungsten matrix composites reinforced with ZrC particles, Journal of Materials Science. 36 (2001) 4625–4631.
[32] R.P. LINDSTEDT, G. SKEVIS, Chemistry of Acetylene Flames, Combustion Science and Technology. 125 (1997) 73–137. https://doi.org/10.1080/00102209708935656.
[33] A. Paul, J.G.P. Binner, B. Vaidhyanathan, A.C.J. Heaton, P.M. Brown, Heat flux mapping of oxyacetylene flames and their use to characterise Cf-HfB2 composites, Advances in Applied Ceramics. 115 (2016) 158–165.
[34] S. Venugopal, Synthesis and processing of sub-micron hafnium diboride powders and carbon-fibre hafnium diboride composite, PhD Thesis, Loughborough University, 2013.
[35] Leo. Brewer, Thermodynamic Properties of the Oxides and their Vaporization Processes., Chem. Rev. 52 (1953) 1–75. https://doi.org/10.1021/cr60161a001.
[36] S.A. Humphry-Baker, K. Peng, W.E. Lee, Oxidation resistant tungsten carbide hardmetals, International Journal of Refractory Metals and Hard Materials. 66 (2017) 135–143. https://doi.org/10.1016/j.ijrmhm.2017.03.009.
[37] J. Walczak, I. Rychłowska-Himmel, Phase equilibria in the systems Fe2O3-WO3 and FeVO4-WO3, Thermochimica Acta. 221 (1993) 115–121. https://doi.org/10.1016/0040-6031(93)80528-I.
[38] A. Ozturk, B.M. Cetegen, Experiments on ceramic formation from liquid precursor spray axially injected into an oxy-acetylene flame, Acta Materialia. 53 (2005) 5203–5211. https://doi.org/10.1016/j.actamat.2005.08.001.
[39] H. Wang, T. Webb, J.W. Bitler, Study of thermal expansion and thermal conductivity of cemented WC–Co composite, International Journal of Refractory Metals and Hard Materials. 49 (2015) 170–177.
[40] S.A. Humphry-Baker, J.M. Marshall, G.D.W. Smith, W.E. Lee, Thermophysical properties of Co-free WC-FeCr hardmetals, Proceedings of the 19th International Plansee Seminar, Reutte, Austria. (2017) HM 19.
[41] P. Peshev, Z. Zakhariev, K. Petrov, The composition and oxidation resistance of coatings deposited on hard carbide alloys using TiB 2, Journal of the Less Common Metals. 67 (1979) 351–356.
[42] P.E. Blackburn, K.F. Andrew, E.A. Gulbransen, F.A. Brassart, Oxidation of Tungsten and Tungsten Based Alloys, WESTINGHOUSE ELECTRIC CORP PITTSBURGH PA, 1961.